Superconducting Cyclotron General Description

H. Blosser, D. Johnson, D. Lawton,
P. Marchand, P. Miller, M. Gordon,
F. Marti, J. Bishop, MSU
J. Purcell, R. Niemann, Argonne National Laboratory
R. Burleigh, Berkeley, CA
J. Riedel, Elkins, AR

In June of 1975, the Laboratory received funds allowing it to move forward with an accelerator development program the goal of which is to build and test a full-scale prototype magnet for a 500 MeV superconducting cyclotron. Since the magnet is the only superconducting element in such a cyclotron, this step of itself largely suffices in establishing basic feasibility of the full cyclotron.

The general layout of the cyclotron involves a solenoid-like circular coil similar in many ways to superconducting coils now in use on several large bubble chambers.[1] With such a coil, magnetic fields of 50 kilogauss are feasible which is about three times higher than typical in present cyclotrons, and the energy from a structure of given physical size is then nearly ten times higher. Thus the 500 MeV cyclotron magnet is approximately the same overall size and weight as the present MSU 56 MeV cyclotron magnet. The attractive features of such a cyclotron are small size and low cost. (In particular the total cost of the 500 MeV magnet is about $1 million of which $750,000 is for construction and $250,000 is for engineering.)

The project is similar in broad features to superconducting cyclotron projects at Chalk River[2] and at the University of Milan.[3] On a detailed level the projects are however rather different both in basic goals and in construction details. In particular our project stresses strong focusing in order to increase the energy of light ion beams and also it includes an interchangeable central geometry so that the magnet can eventually be used either as a conventional cyclotron with internal source or as a booster accelerator.

The coil design for the MSU magnet uses a layer-type winding which is more compact and less expensive than the pancake windings which have thus far been used in bubble chamber magnets. The basic cyclotron layout is a dee-in-valley design with three sectors and three dees. Major features can be seen in Figs. 1 and 2 which are a section view of the complete cyclotron and a perspective view of the magnet. A listing of major parameters is given in Table 1.

At the present time, the prototype magnet is in the midst of construction. Steel castings for the yoke have been completed, and Fig. 3 shows the assembled yoke set up for factory inspection. The outer cryostat vessel is also complete; the inner cryostat vessel has unfortunately been delayed and is now expected in late August. Conductor for the coil is now in-house in East Lansing so that coil winding will start as soon as the inner cryostat vessel is available. (This vessel is also the coil form.) The refrigeration unit has likewise been received after successfully completing factory tests; it is now being connected up and should be ready for operation in late August.

The overall project schedule presented in our original proposal estimated the first magnet turn-on would come 20 months after funding. At the present time it appears we have an excellent chance of meeting this schedule and some chance of getting to the first turn-on one or two months earlier than anticipated.

Assuming the magnet performs as expected, we hope to proceed without significant delay with construction of the other components required to make the magnet into a complete cyclotron in order to verify beam characteristics. The expected performance of the magnet using an internal ion source is shown in Fig. 4. Even in this basic configuration, the cyclotron is clearly an exceptionally attractive instrument for nuclear research.

REFERENCES

1. J. Purcell, Superconducting Magnet System for the 12 foot Bubble Chamber, Argonne report ANL/HEP 6813 (1968).
2. J.H. Ormrod, C.B. Bigham, J.S. Fraser, E.A. Heighway, C.R. Hoffmann, J.A. Hulbert, H.R. Schneider and Q.A. Walker, The Chalk River Superconducting Heavy Ion Cyclotron, Proc. 7th Int. Conf. on Cyclotrons and their Applications (Birkhäuser, Basel, 1975), p. 595-599.
3. F. Resmini (private communication).

Table 1: Parameter Sheet--500 MeV Cyclotron Magnet

Coil:		
# of turns	short coils	36 layers x 32 turns/layer = 1152
	long coils	36 " x 64 " " = 2304
	total 4 coils	= 6912
Nominal current density	coil avg.	3,500 amps/cm^2
	conductor	5,000 amps/cm^2
Conductor size		0.110"x0.196" = 2.8mmx5.0mm
Design current		700 amps
Stored energy (with iron yoke)		16.9 Mjoules
Inductance (full field)	short coils	13.8 Henry
	long coils	27.6 "
	mutual	13.8 "
Basic winding dimensions		
Radial		60" I.D., 71" O.D. (Δr=5.5")
Axial	median plane to small coil	1.425"
	small coil ht.	6.465"
	small coil to large coil	.375"
	large coil ht.	12.930"
	total overall	42.390"
Magnet Yoke		
	Nominal weight	190,000 lbs.
	Maximum size	120" dia x 86" high
	Material	cast 1020 steel
Magnetic Field:		
	Average field at extraction radius	4.95 tesla
	Max. hill field	5.9 tesla
	Max. field in winding	4.4 tesla
	Bρ (at extraction radius)	3.22 tesla-meter
	Magnet bending limit	E=500 MeV (Q^2/A)
	Magnet focusing limit	E/A=160 MeV (Q/A)
Refrigerator		
CTI 1400 with 2 compressors		
closed metal system (no gas bag)		

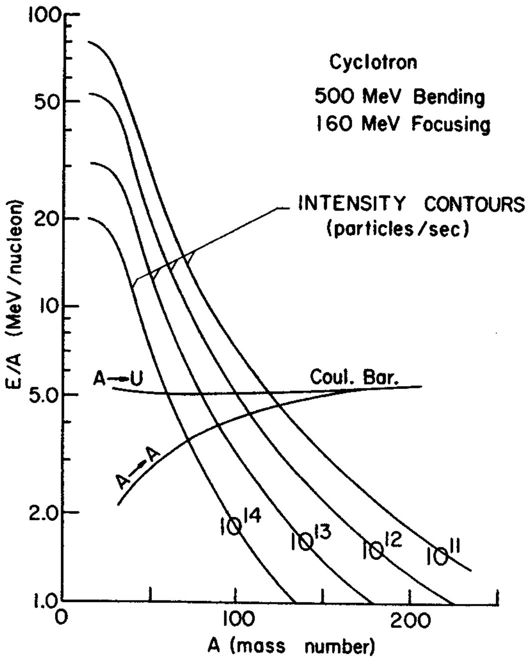

Fig. 4. Maximum energy per nucleon versus mass number for the 500 MeV cyclotron. Intensity contours correspond to an internal source of the type presently used in heavy ion cyclotrons.

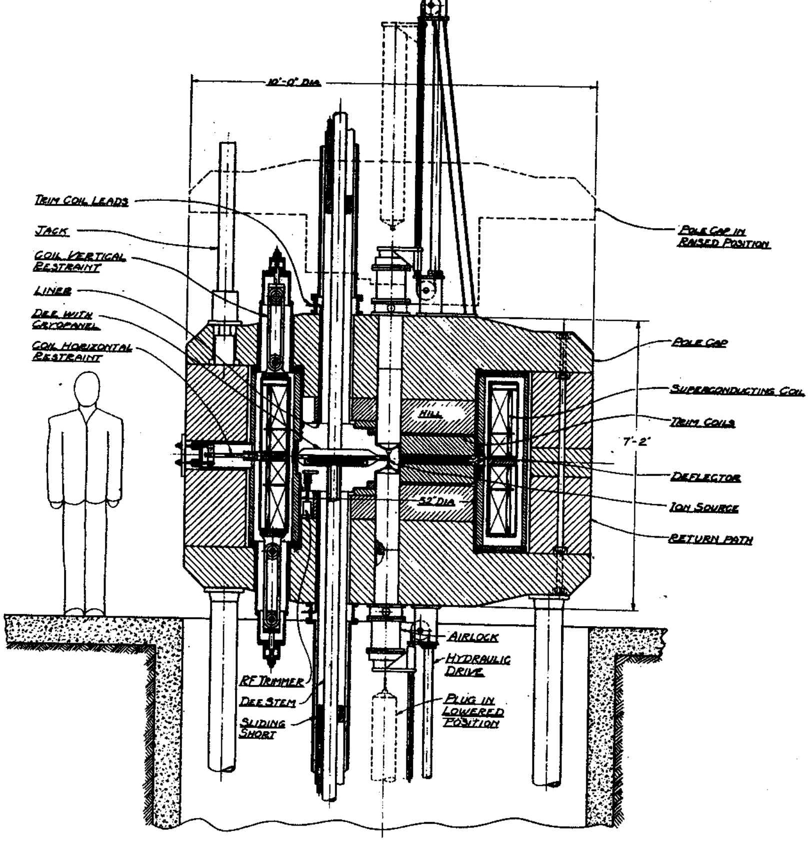

Fig. 1. Vertical section view of the 500 MeV cyclotron.

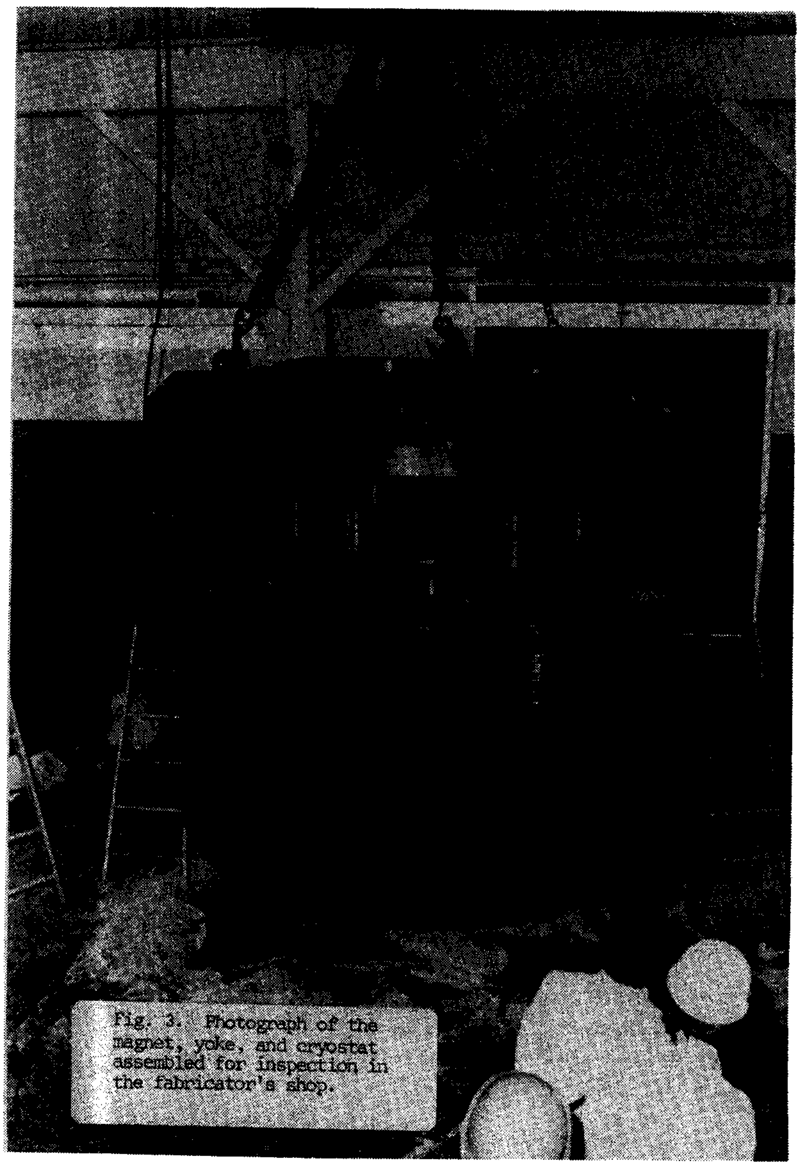

Fig. 3. Photograph of the magnet, yoke, and cryostat assembled for inspection in the fabricator's shop.

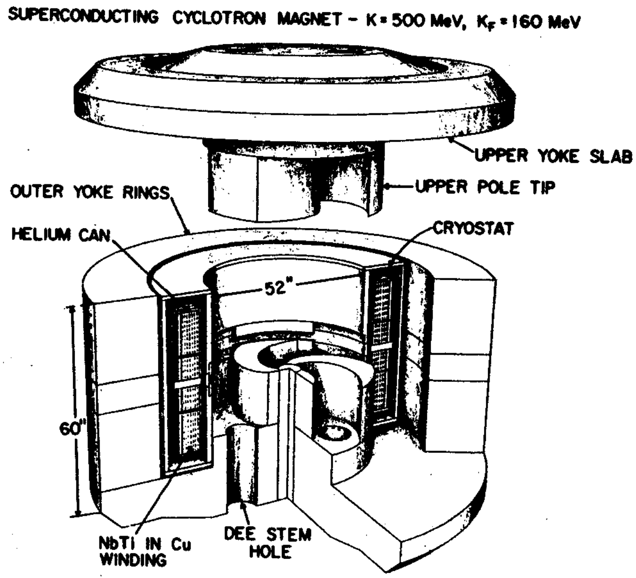

Fig. 2. Perspective view of the magnet for the 500 MeV cyclotron.

Field Calculations for 500 MeV Magnet

D. Johnson, H. Blosser, and M. Gordon

The cyclotron magnet consists of a cylindrically symmetric yoke plus an array of iron ridges (and holes) with 120° symmetry. The magnet operates at high fields where the steel is approximately fully saturated. The magnetization of cylindrically symmetric magnets can be fully calculated using relaxation codes[1] (in practice this is limited by round-off errors related to grid size and computation time). A reasonable approximation for the nonazimuthally symmetric parts of the magnet is to assume that all magnetic moments are at their saturation value and pointed in the Z direction (parallel to the axis of the magnet). The accuracy of this approximation can be inferred by computing the field of a cylindrically symmetric magnet and comparing results of complete relaxation calculations vs. results of calculations done with a mixture of relaxation and constant M_z. Figure 1 shows the relaxation grid used for a "Trim" calculation of a cylindrically symmetric magnet. In Fig. 2, the solid curve shows the median plane field predicted by this calculation. For comparison the dashed curve in Fig. 2 shows the field obtained using the alternate calculation system where the pole tips (the grey area of Fig. 1) are removed from the Trim calculation and are then added back using the approximation that the magnet moments are fully saturated and aligned in the Z direction. The two calculations are seen to agree quite closely.

Accepting the approximate accuracy of the procedure of replacing ridges of steel near the median plane by equivalent charge arrays, we can then proceed to calculate structures with ridges oriented in any arbitrary way and in particular in the spiral array needed for the cyclotron magnet. Figure 3 is a contour map of the median plane field obtained from this calculation. This field is used to compute orbits and predict performance of the cyclotron.

The computing procedure can also be used to evaluate the magnet field inside the coil. Table 1 gives a numerical printout of B_z and B_r over a grid of r and z values covering the small coil and the large coil (this particular grid is for the cylindrically symmetric magnet shown in Fig. 1). Computing limitations unfortunately leave a sawtooth-like residual error so that averaging values from line to line is necessary. The maximum field in the coil is seen to be approximately 44 kilogauss.

[1]J.S. Colonias, TRIM - A magnetostatic computer program for the CDC 6600. UCRL-18439. Lawrence Berkeley Lab, 1968.

Magnetic Field in coil (gauss): upper number axial, lower number radial. Amp turns 2 x 2,313,100

height (inches) \ radius (inches)	30.000	30.917	31.833	32.750	33.667	34.583	35.500
20.500	27709.0	24590.7	19928.9	14940.0	9993.3	5191.6	1717.6
	20804.0	24219.7	26948.9	27128.3	26816.5	25374.0	22309.6
19.500	30826.1	25752.1	19603.9	13577.3	7504.2	1240.5	-1998.8
	21441.7	23344.7	24166.7	24080.5	23103.1	21105.0	17955.1
18.500	35263.6	30871.4	23829.3	15937.5	9976.7	2753.4	-2935.6
	16659.5	18732.5	20077.9	20741.5	20726.1	20071.8	13915.0
17.500	36176.2	29989.0	22340.7	14820.0	7255.6	-502.9	-4965.8
	15430.3	15429.3	16951.4	17012.5	16641.1	15910.5	14775.5
16.500	39145.1	34135.0	26059.3	18133.6	10152.4	2044.8	-4370.9
	12290.3	13552.6	14286.7	14708.8	14801.3	14587.6	14149.6
15.500	39222.9	32509.6	24177.4	15916.7	7639.3	-724.0	-5749.7
	11065.7	11675.9	12029.0	12153.9	12068.0	11805.6	11388.4
14.500	41572.3	36165.7	27632.5	19157.9	10679.0	2140.9	-4645.6
	8789.2	9590.3	10035.6	10325.5	10456.1	10438.9	10311.9
13.500	41121.2	34117.8	25447.3	15831.9	8216.6	-446.6	-5763.4
	7637.2	7994.9	8229.7	8367.2	8414.0	8378.1	8295.3
12.500	43020.0	37413.9	28664.9	19971.9	11282.0	2546.8	-4438.7
	5916.5	6330.3	6552.2	6728.4	6861.9	6954.2	7014.0
11.500	42119.9	35013.2	26244.9	17535.9	8829.7	71.1	-5381.4
	4663.1	4784.3	4901.9	5033.3	5178.6	5329.2	5514.0
10.500	43565.9	37933.7	29222.9	20565.6	11906.4	3190.3	-3841.3
	3367.1	3333.9	3290.0	3340.7	3471.5	3679.1	3972.3
9.500	42086.0	35135.0	26563.9	18018.0	9483.7	981.7	-4465.0
	1735.9	1500.7	1499.4	1628.7	1886.6	2380.4	3071.4
8.500	42552.1	36953.2	28653.8	20236.0	11833.3	3595.9	-2618.8
	2542.6	3081.0	2893.6	2919.5	3023.0	3163.3	2624.0
8.000	42176.6	36108.3	27910.2	19526.9	11133.1	2862.7	-2609.6
	2288.5	2669.2	2834.9	2962.6	3041.0	2913.3	2588.7
7.527	42888.6	37107.2	28757.8	20337.6	11903.8	3482.9	-2604.4
	1714.8	2503.9	3030.2	3254.6	3386.0	3405.8	3058.9
7.054	42788.2	36483.2	27993.9	19525.8	11039.0	2498.5	-3127.9
	1635.9	2026.0	2250.2	2389.8	2426.9	2255.3	1957.8
6.580	43437.7	37594.9	29053.6	20551.4	12018.4	3383.5	-2851.9
	486.6	890.7	1187.3	1399.7	1554.0	1635.8	1599.4
6.107	43133.2	36818.4	28250.9	19730.0	11173.7	2499.4	-3183.9
	88.0	298.4	484.9	652.0	789.4	874.6	961.7
5.634	43619.4	37823.2	29262.1	20744.0	12185.6	3498.0	-2771.3
	-929.5	-708.7	-567.9	-399.0	-206.7	.1	203.4
5.161	43185.5	36942.0	28408.7	19919.3	11352.4	2707.9	-2073.8
	-1495.5	-1411.0	-1267.7	-1058.4	-788.5	-478.3	-63.3
4.687	43565.4	37861.1	29370.5	20927.9	12441.1	3805.6	-2438.9
	-2514.5	-2384.6	-2357.0	-2228.7	-1987.6	-1633.4	-1191.9
4.214	43038.9	36894.0	28467.5	20099.9	11692.0	3121.4	-2509.7
	-3172.0	-3193.6	-3096.3	-2840.6	-2417.2	-1854.7	-1073.0
3.741	43348.8	37727.1	29372.1	21103.8	12805.8	4334.6	-1826.0
	-4261.6	-4159.5	-4255.3	-4188.5	-3901.6	-3375.6	-2638.2
3.268	42754.8	36659.9	28402.0	20267.9	12121.4	3793.9	-1721.0
	-4933.9	-5115.4	-5105.3	-4816.7	-4216.5	-3315.8	-2030.0
2.795	43009.3	37354.4	29216.6	21251.4	13295.9	5157.9	-809.2
	-6028.4	-5992.4	-6334.5	-6394.4	-6090.1	-5373.8	-4210.5
2.321	42311.0	36109.4	28138.9	20392.2	12676.6	4863.3	-419.3
	-6683.3	-7261.8	-7421.9	-7144.6	-6370.0	-4945.1	-2849.4
1.848	42194.5	36451.8	28815.4	21317.3	13894.9	6473.4	921.0
	-6642.6	-7723.4	-8735.9	-8999.3	-8741.4	-7900.6	-6032.9
1.375	41031.3	35020.8	27964.2	20646.1	13568.5	5849.9	1897.5
	-7511.2	-8416.5	-8670.4	-8391.5	-7459.4	-5167.0	-2440.4
$\int B_r dZ$ (gauss-inch)	103942.7	114307.4	120025.4	123486.7	124912.3	124577.4	122039.8

Table 1. Magnetic field in the superconducting coil in gauss at various distances from the median plane (height) and at various radii. For each entry the upper number is the axial component of the field and the lower number the radial component of the field.

NOTE ADDED IN PROOF: The text incorrectly states that the fields in Fig. 2 correspond to the magnet outlined in Fig. 1. The fields shown in Fig. 2 are for an earlier magnet with a solid 12" diameter center tip as contrasted with the hollow center shown in Fig. 1. The magnet and trim grid shown in Fig. 1 go with the computation of coil fields shown in Table 1.

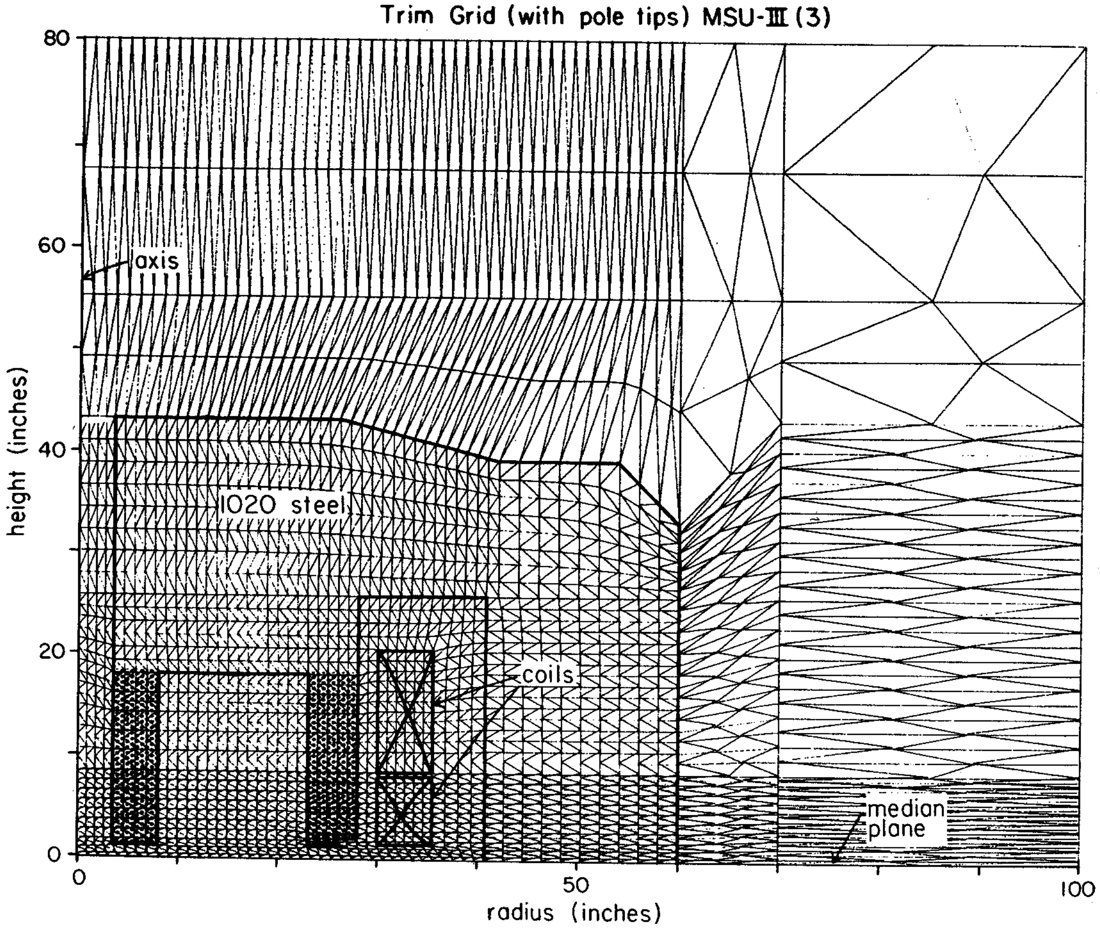

Fig. 1. · Relaxation grid used for computing the magnetic field of a cylindrically symmetric magnet as outlined by the heavy black lines.

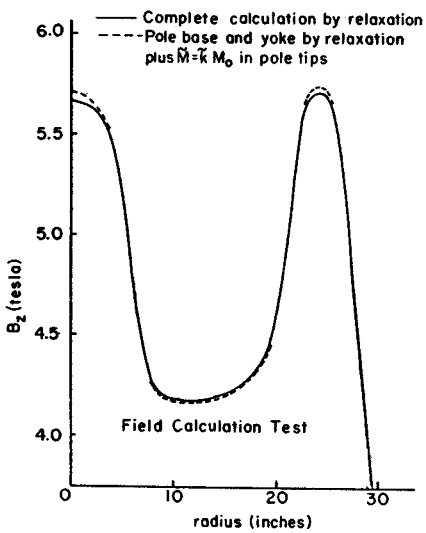

Fig. 2. Magnetic field in the median plane as computed by program TRIM for the magnet shown in Fig. 1 (solid curve) and as computed with the pole tips (the grey area in Fig. 1) replaced by fully saturated iron (dashed curve).

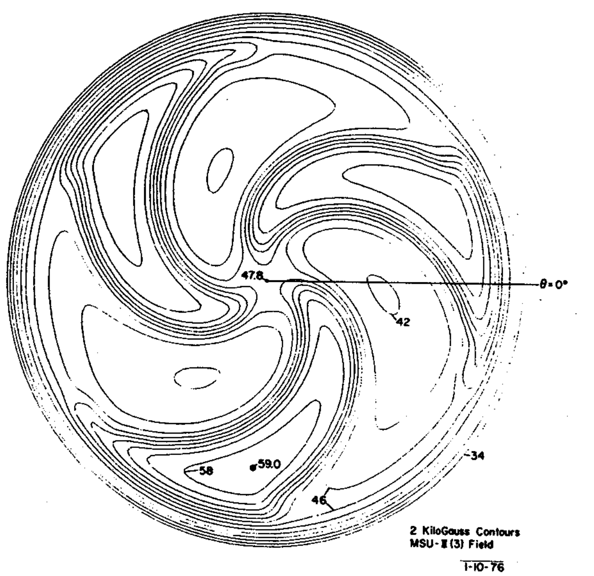

Fig. 3. Predicted median plane magnetic field for the 500 MeV magnet. The calculation uses the approximation employed in obtaining the dashed curve in Fig. 2.

Superconducting Coil Internal Structure

H. Blosser, D. Lawton, MSU
J. Purcell, R. Niemann, Argonne National Laboratory

The basic coil structure is a layer type winding, i.e. a winding which first progresses in the axial direction at constant r, then climbs to a new r value and returns in the opposite sense in the axial direction. This is a type of winding generally used on small coils and contrasts with the pancake winding which has been more common on large coils. The advantages of layer type winding are lower fabrication costs i.e. winding jigs and handling jigs are eliminated and better space factor i.e. no need for clamping bolts, etc. The MSU coil will thus be directly wound onto a stainless steel bobbin on which it will permanently remain. After winding, the outer periphery of this bobbin will be covered with stainless steel and welded so that the bobbin becomes the helium can for the cryostat. The conductor is a composite structure as shown in Fig. 1 (fabricated by Intermagnetics General Corporation). The manufacturer was able to furnish the conductor in lengths of approximately 10,000 feet which implies a total of ten internal joints.

Two different joint techniques are currently being considered. One of these is a simple overlap of the conductor inside a rectangular copper sleeve with soft solder and crimping. A joint of this type is bulky and must be located in the insulating plate at the end of the layer, but it is easy to make (30 minutes) and strong (stronger than the conductor). The alternate technique involves unbraiding of the stranded cable, scarfing and silver soldering of the central copper core and rebraiding and soldering of the copper strands. This type of joint then has the same cross section as the normal conductor and can therefore be located anywhere, but it is slow to make (six hours) and weaker than the normal conductor (breaking strength reduced by 20%).

Cooling for the coil is provided by introducing a "picket fence" between each layer. The pickets are 1 mm thick and 1/2" wide and extend for the length of the coil in the Z direction. Alternate 1/2" azimuthal spaces are empty and constitute the helium passages. Radial helium flow into the pickets is provided by grooves in the insulating plates at each end of the coil.

Turn-to-turn insulation within a layer is formed from U-shaped mylar caps on each end of the conductor as shown in Fig. 2. The creasing of the mylar is done in the winding line, using a heating fixture. On one side of the conductor, a .002" adhesive is introduced between the mylar and the conductor to hold the mylar in place until the next turn is wound (no adhesive is needed on the side of the conductor laying against the previously wound turn). With this insulation system, approximately half of the broad face of the conductor is left bare.

The electrical breakdown resistance of this insulation system is excellent. In a puncture test on twelve samples at 600 volts turn-to-turn, the lowest failure occurred at five times the design maximum turn-to-turn pressure.

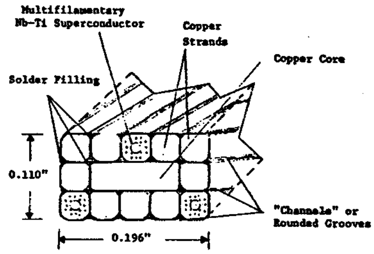

SPECIFICATIONS

Nb-Ti CONDUCTOR

Copper:Superconductor Ratio	2.5:1
Conductor Diameter	~0.035 inches
Number of Nb-Ti Filaments	114
Filament Diameter	1.8 mils
Minimum Filament Spacing	1 mil
Twist Length	2 inches
Composition of Solder Bond	50/50 Sn-Pb

OVERALL CABLE

Copper:Superconductor Ratio	21:1
Total Length	130,000 ft.
Individual Lengths	~10,000 ft.
Dimensions	0.196" ± 0.0015" x 0.110" ± 0.0015"
Corner Radius	~1/32 inches
Surface Finish (on Flat Surfaces)	125µ inches
Design Critical Current at 5.5 Tesla and 4.2°K	900 Amps
Guaranteed Critical Current at 5.5 Tesla and 4.2°K	770 Amps
Twist Length	3 inches
Current Transfer Length	<1 inch
Resistance Ratio [R(300)/R(4.2)]	>180:1
Tensile Loading of Superconductor without Damage to Nb-Ti	≤17,000 psi
Density (Packing Factor)	~88%

Fig. 1. Details of the composite Niobium-Titanium cable.

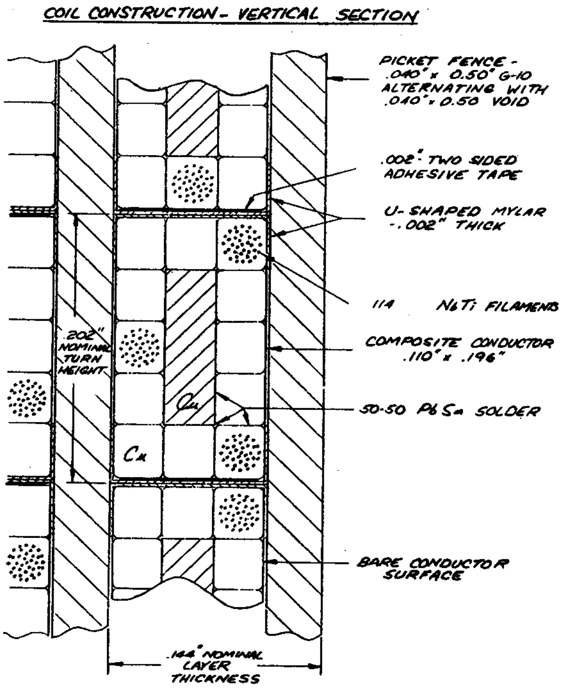

Fig. 2. Details of the insulation system used in the superconducting coil.

Superconducting Coil Internal Stress Calculations

H. Blosser, MSU

and

N. Johnson, Oak Ridge, TN

Internal coil stresses have been calculated by Dr. Neil Johnson of Mechanics Research Incorporated. Only radial forces are included in these calculations, i.e. the code is for an infinitely long solenoid; otherwise the calculation is quite detailed. Results for radial stress and hoop stress are shown in Figs. 1 and 2 respectively. The calculations assume a winding tension of 2,000 psi and a banding tension of 20,000 psi, the banding being of 1-inch radial thickness at the outside of the coil. Stresses are computed after winding, after cooldown, and after field is turned on, and computations were run for both aluminum and stainless steel banding. The stress characteristics of the aluminum banding are very attractive; the banding tension increases in cooldown (in contrast with the stainless steel which decreases) so that the final hoop tension in the conductor when the coil is on is considerably lower with the aluminum banding. Eddy currents in the aluminum banding are relatively small due to the high 4.2° resistance of the 6061 alloy.

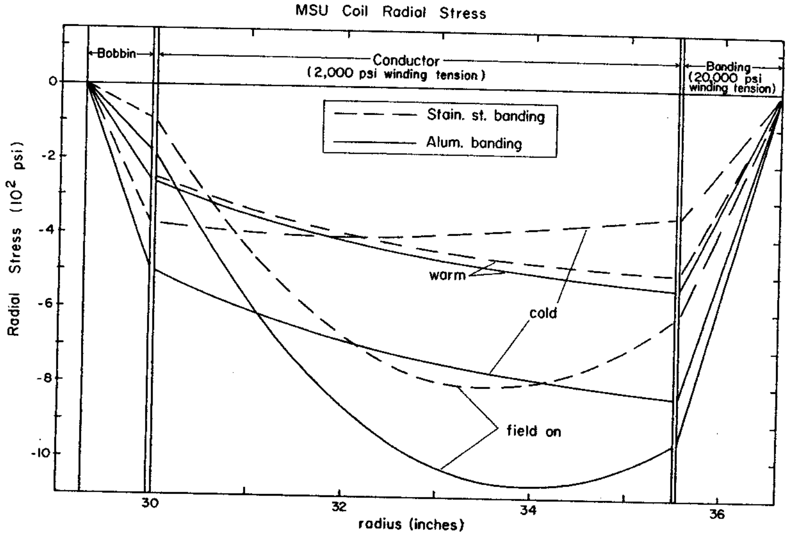

Fig. 1. Radial compression in the superconducting coil in the three conditions warm, cold, and field-on. Note that the stress remains negative at the boundary between bobbin and conductor even when the field is on, thereby indicating that the prestresses in winding and banding are sufficient to keep the coil from lifting off the bobbin when the field is turned on.

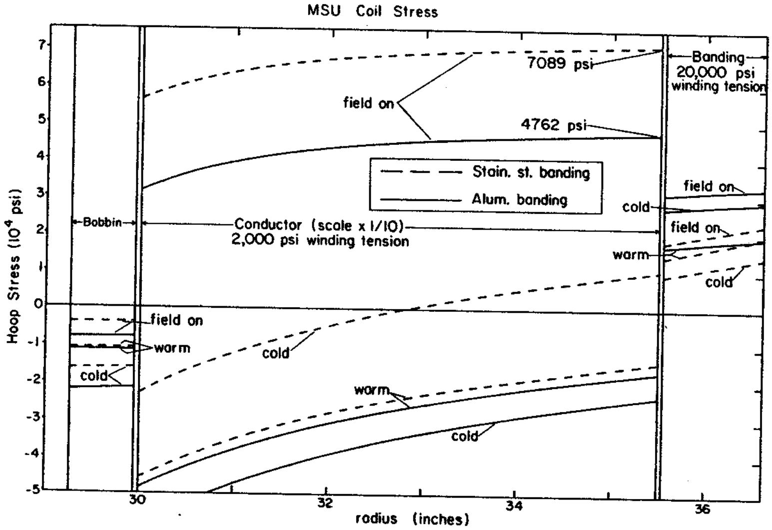

Fig. 2. Azimuthal stress in the superconducting coil for the same conditions as in Fig. 1. Note that the stress scale is expanded by x 10 in the radial interval from 30" to 35.5" (the region occupied by the winding).

Superconducting Coil Support System

H. Blosser and M. Gordon, MSU
S. Wang, Argonne

The main coil support will be provided by nine tension members, three pulling up, three pulling down, and three pulling radially out. (In addition there are two very small azimuthal tension members.) This support system must carry the weight of the coil (~15,000 lbs.) and in addition must provide an adequate spring constant to overcome the instabilities associated with the unstable equilibrium of the large magnetic force on the coil.

Estimating the magnitude of the unstable magnetic force is difficult. An earlier approximate estimate by S.T. Wang gave 510,000 lbs. per inch for the vertical force and 27,000 lbs. per inch for the radial force. Wang's approximation involved replacing the magnet with an array of six dipoles.

For a cylindrically symmetric magnet, the vertical force can also be calculated from the relaxation code since the magnet is still axially symmetric when the coil is displaced vertically (although median plane symmetry is lacking). Unfortunately the force comes computationally from the difference in magnetic energy at several coil positions; this is a small number and hence sensitive to the round-off errors in the relaxation code; the numerical result for the vertical force using this procedure is 160,000 lbs. per inch. (The radial force cannot be computed by this technique.)

M.M. Gordon has used still a third procedure for estimating the vertical force, namely, to take the magnetic field from the Trim program, subtract off the field produced by the coil to obtain the field produced by the iron, and assume the force between the iron and the coil is given by evaluating $i\vec{B} \times \widehat{Dl}$ over the coil. Again the procedure is bothered by round-off errors in the Trim program; the numerical result is 80,000 lbs. per inch for the vertical spring constant.

Gordon also notes that if the iron is equivalent to a simple dipole located at the coil center, then the vertical spring constant will be twice the radial spring constant and of opposite sign, i.e. if the coil was unstable vertically it would be stable radially and vice versa.

In view of the difficulty of estimating both the spring constant and the maximum likely displacement, it was decided somewhat arbitrarily to design the vertical support links on the basis of a breaking strength of 125,000 lbs. total for three links, and the radial support links on the basis of a breaking strength of 15,000 lbs. for each link individually. In addition each link will be provided with a strain gauge which will be monitored as the magnet is gradually turned on so that position adjustments can be made before forces approach a dangerous level.

The actual support links proper will be fabricated from an Epoxy glass laminate in the fashion of the support links in the SSR magnets at Argonne. Taking the ratio of strength to heat leak as a figure of merit, the Epoxy glass laminate is approximately three times better than stainless steel. Construction details for a typical link are shown in Fig. 1 (next page).

Cryogenic Stability of Superconducting Coil

H.G. Blosser, M.S.U.

Cryogenic stability is achieved by incorporating relatively large amounts of copper into the conductor, namely a copper to superconducting ratio of 21 to 1. No actual cooling experiments have been performed on this conductor but comparison with experiments done at M.I.T. for the Argonne U-25 magnet indicates that the design current is well below the thermal recovery limit. This comparison is outlined in Table 1.

Table 1. Cryogenic Stability Review

Infer from MIT U-25 tests[1]

0.040" pickets reduce critical current by 20%

.002" Mylar reduces critical current by 50%

Effective cooling surface width U-25

0.2 cm x 2 = 0.4 cm

Effective cooling surface width MSU (½ of 5 mm surface bare, ½ covered with .002" Mylar, .040" deep cooling channels)

0.5 cm x ½ x 2 x 0.8

\+ 0.5 cm x ½ x 2 x 0.5 x 0.8 = 0.4 cm + 0.20 cm = 0.60 cm

\+ ~ small contribution

Both magnets $J_{cond.} = 5{,}000$ amps/cm^2, $\rho \simeq \frac{\rho 300^\circ}{150}$

Power/unit length = $I^2 \rho / A = IJ\rho$

Figure of merit:

$$\frac{\text{Cooling area/power}_{MSU}}{\text{Cooling area/power}_{U\text{-}25}} = \frac{(IJ\rho)_{U\text{-}25}}{(IJ\rho)_{MSU}} \frac{\text{area MSU}}{\text{area U-25}}$$

$$= \frac{700}{1000} \times \frac{0.4}{0.6} = 0.467$$

i.e. cooling area/watt for MSU is approximately double that for U-25

If conduction cooling along wire is important, figure of merit is power/unit area/length = power/volume

$$P/\text{volume} = \frac{I^2 R}{A \ell} = J^2 \rho$$

MSU and U-25 alike on this criterion.

[1]Y. Iwasa (private communication)

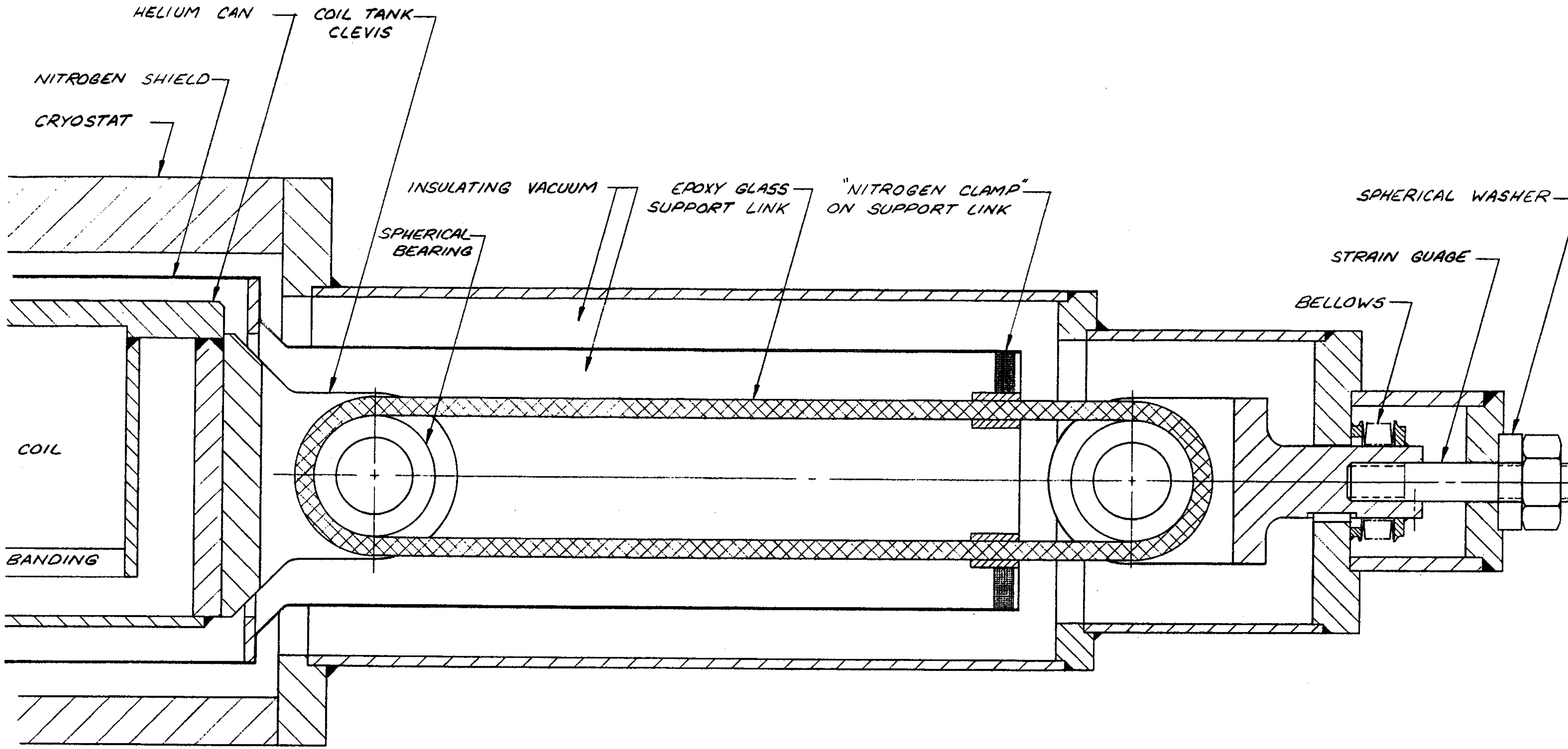

Fig. 1. Drawing of a typical vertical support link for the superconducting coil. The epoxy glass support link is ½ inch thick by 1½ inches wide. Horizontal support links are similar but smaller.

Safety Systems and Dump Circuits

Peter Miller and M.M. Gordon

1. Introduction

Shaping of the cyclotron field to match various particles requires dividing the main winding into two independently powered sections; this gives a dump circuit complexity not usually present in superconducting magnets. In particular a rapid drop in the current in one coil pair will tend to give a sharp increase in the current in the other pair through the mutual inductance. The energy dump circuit can be designed so that the current does not exceed the design limit.

The power supply and energy dump system are shown schematically in Fig. 1. Some experience with the magnet will be required to develop a suitable automatic fault detector. Initial testing will be with a manually activated dump. Signals that will be monitored will include the difference between the voltages across the coil halves (shown) and some analysis of dB/dt from pickup coils. The power supplies will be disconnected when a fault occurs. An analysis of the temperature of the wire and the pressure in the cryostat has been published for the magnet called BIM.[1] which is electrically a single circuit. We have extended this treatment to the case of present interest, taking account of the magnetic coupling between the coils. A further complication is that the inductances of the MSU magnet, which uses iron poles and yoke, are found to vary with excitation. An analysis using constant effective values of the inductances is sufficiently accurate and is used to represent the magnet for the present purpose.

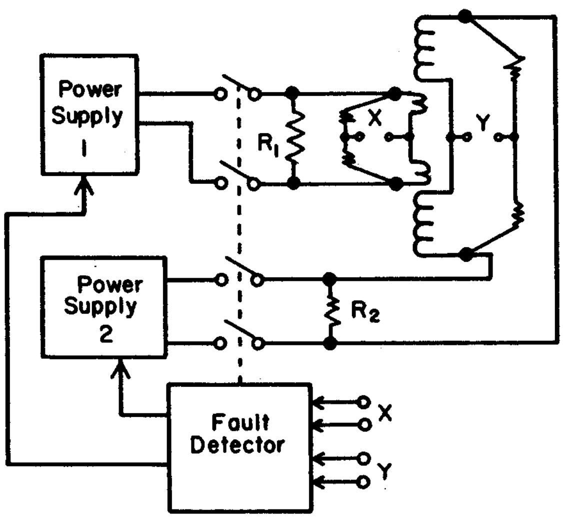

Fig. 1.--Schematic diagram of the dump circuitry.

2. Choice of Resistors

Each of the two coils is connected to its energy dump resistor (R_1,R_2). The self-inductances, L_1 and L_2, and the mutual inductance M are assumed to be constant. The differential equations for the currents (i_1,i_2) are:

$$-i_1R_1 = L_1 \frac{di_1}{dt} + M \frac{di_2}{dt}$$

$$-i_2R_2 = L_2 \frac{di_2}{dt} + M \frac{di_1}{dt} .$$

Asymptotically, i.e., after a transient has decayed away, the currents become proportional to an exponential function:

$$i_1 = A\, e^{-\lambda t}$$

$$i_2 = b\, i_1, \text{ (b is constant).}$$

From the differential equations we obtain the relation between b and λ, which is independent of the initial conditions:

$$\lambda = \frac{bR_2}{bL_2+M} \text{ if } b \geq 1 \text{ and } \lambda = \frac{R_1}{L_1+Mb} \text{ if } b \leq 1.$$

Since the coils will be operated at equal currents for maximum excitation, b should be chosen close to 1. Otherwise, when a dump occurs one of the currents will for a time rise above the maximum operating current which will place extra thermal, magnetic and mechanical stress on the coil. For b=1 we obtain

$$\frac{R_1}{R_2} = \frac{L_1+M}{L_2+M}, \text{ and } \lambda = \frac{R_1}{L_1+M}.$$

The tolerance on R_1/R_2 to insure that i_1 and i_2 decrease initially is ±25% if $i_1=i_2$ initially. In view of this wide tolerance it is practical to measure $i_1(t)$ and $i_2(t)$ in a sequence of test dumps and then trim R_1 as required.

The values of R_1 and R_2 determine the maximum voltage applied to the coil.

$$i_1R_1 = V_1$$

$$i_2R_2 = V_2$$

The dielectric strength of helium gas in a superconducting magnet is 200 v/mm, and 1/5 of this, or 40 v/mm is considered a good design criterion. The maximum coil voltage design value of 200 v leads to the requirement that the minimum effective spacing of the coil leads be at least 5 mm. The voltage gradient between layers of the coil is about 7 times smaller than the estimate for the leads. Since $L_2>L_1$, V_2 reaches the limit.

$R_2 = \frac{200V}{700A} = .2857$ ohm.

With the inductances determined as shown in Section 3 (L_1=13.8 H, L_2=27.6 H and M=13.8 H) one obtains R_1= .1905 ohm and $\frac{1}{\lambda}$ = 144.9 sec.

3. Determination of Inductances

3.1.--Analysis of stored energy

The relaxation program TRIM obtains the magnetic induction B and the magnetic intensity H everywhere on a grid representing the magnet and the space surrounding it, and it therefore can provide the total magnetic stored energy which is related to the inductances and the currents. In normal operation the iron of the magnet in and near the coils will be saturated and the inductances would be expected to be fairly close to the values obtained with air core coils, the extreme high field limit of the inductances. These air core values were calculated exactly by first obtaining the vector potential for a suitable set of currents in the coil and then calculating the inductances from the flux changes. These values are 11.43 H, 25.48 H and 11.34 H for L_1, L_2, and M, respectively.

The total magnetic energy was calculated with TRIM at 14 different combinations of currents in the two coils (Table 1). Most of these pairs were chosen to divide the (i_1,i_2) plane into successively smaller squares. The average value of the inductances L_1, L_2, and M were calculated on each square by replacing differentials by finite differences in the definitions:

$$dE = (L_1 i_1 + M i_2) di_1 + (L_2 i_2 + M i_1) di_2$$

$$= \frac{\partial E}{\partial i_1} di_1 + \frac{\partial E}{\partial i_2} di_2,$$

and $$M = \frac{\partial^2 E}{\partial i_1 \partial i_2}.$$

The results give a rather non-uniform variation of the inductances with excitation which is suspected to result from the limited accuracy of the computed energies from TRIM. When this analysis is done, the two self-inductances, L_1 and L_2, always turn out several henries larger than the air core values, whereas M is the same as or up to 3 henries less than the air core result.

Another approach is to adjust L_1, L_2 and M in the energy equation

$$E_c = \frac{1}{2}(L_1 i_1^2 + L_2 i_2^2 + 2M i_1 i_2) \qquad (1)$$

in order to fit 3 calculated energies. When this is done with the available TRIM data the inductances vary greatly from case to case, sometimes becoming negative. This is also interpreted as a sign of the limited numerical accuracy of the computed energies. One triple gives a solution which compares favorably with the air core calculation, namely

$$L_1=14.9 \text{ H}, L_2=29.8 \text{ H and } M=14.9 \text{ H}. \qquad (2)$$

TABLE I.

Label	i_1(kA)	i_2(kA)	E(Mj)
1	.7	.7	16.90
2	.525	.525	10.26
3	.7	.525	12.76
4	.525	.7	14.30
5	.350	.7	11.86
6	.7	.350	9.12
7	.35	.35	5.06
8	.21	.21	2.16
9	.525	.35	6.91
10	.35	.525	8.08
11	.7	0.	3.93
12	.35	0.	1.11
13	0	.7	7.90
14	0	.35	2.49

This solution corresponds to solving Eq. 1 at the points labeled 2, 5 and 6 in Table I. We conclude that the only reliable data we have for estimating the individual inductances are the air core values. The total magnetic energy calculated by TRIM is probably accurate to better than 15% and so sets a constraint on the actual inductances, but the information is not accurate enough to allow a straightforward solution. Based on the analysis of the next section we adopt for design purposes inductances which give the calculated stored energy at full excitation and whose relative values are the same as given by Eq. 2.

3.2.--Equal Currents in the Two Coils

As discussed in Section 2, ratio R_1/R_2 is chosen to make $i_1=i_2$ asymptotically during a dump.

If $i_1=i_2=i$, Eq. 1 can be reduced to

$$E_c = 1/2 \, L_0 \, i^2, \qquad (3)$$

with

$$L_0 = L_1 + L_2 + 2M. \qquad (4)$$

Even if the inductances vary we deine L_0 by this same relation

$$L_0(i) = \frac{2 \, E(i)}{i^2}. \qquad (5)$$

In Fig. 2, E is plotted as a function of i^2 together with Eq. 3 for two values of L_0 which correspond (through Eq. 5) to the two data with highest excitation (points 1 and 2 in Table 1).

The effective inductance λ for small changes in current is not L_0 but is twice the slope of the curve:

$$\lambda = 2 \frac{dE_c}{d(i^2)}. \qquad (6)$$

By differentiating the dashed curve in Fig. 2, we obtain λ as a function of i^2, shown in Fig. 3. The heights of the rectangular areas drawn to represent the areas under the curve are equal to the values of L_0 shown in Fig. 2, since

$$L_0 = \frac{1}{i^2} \int_0^{i^2} \lambda(i^2)\, d(i^2).$$

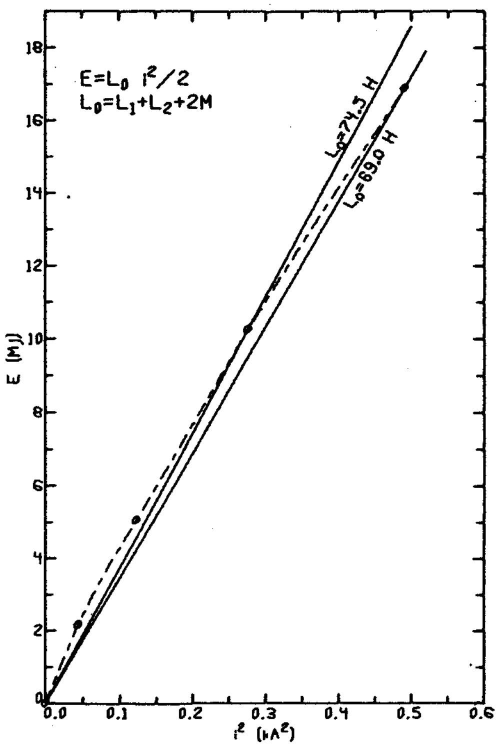

Fig. 2.--Total energy stored in the magnetic field vs. current squared, when the currents in the two coils are the same. The solid lines represent two different constant values of the total inductance; the circles and the interpolated dashed curve refer to the MSU magnet design.

3.3.--Discussion

The choice of L_0=69 H as an approximate representation of the total inductance can be understood as follows. By referring to Fig. 3 one sees that L_0 would then exceed the actual incremental inductance λ for i^2>0.15. Thus, the decay time will be overestimated at large currents. The calculated stored energy E_c will, however, be less than the actual energy E for all i^2<.49, that is over the entire operating range. At i^2=.49 we have $E=E_c$, by the choice of inductance values. In the calculation of the amount of heat produced in the coil during a dump, these two errors tend to offset each other. In view of this and their separate magnitudes (~10%) we have adopted L_0=69 H. Therefore, we renormalized the inductances obtained at 75% excitation (Eq. 2) to yield this value of the sum (Eq. 4).

4. Dump Calculations

If the dump resistors are matched to the coil inductances, the worst condition for overheating

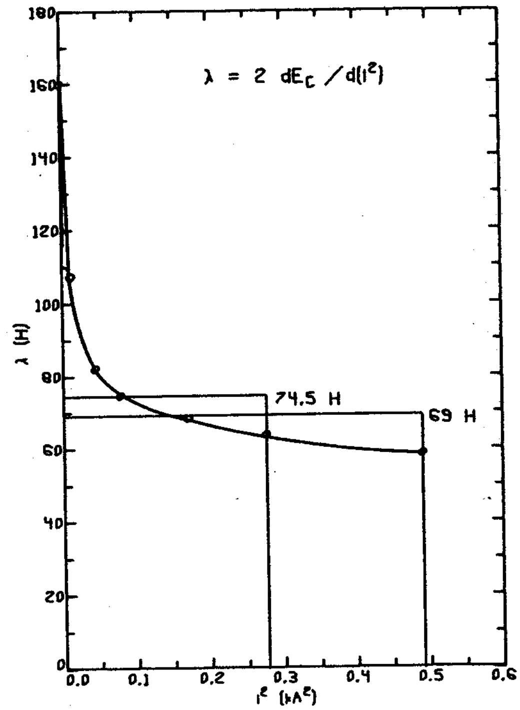

Fig. 3.--Incremental inductance (effective inductance for small current changes) vs. current squared, obtained by differentiation of Fig. 2.

the conductor occurs when both coils are carrying the maximum current. If a small section of conductor looses all thermal contact with the helium bath and goes normal, its final temperature becomes very high unless the dump system is designed for very high voltage operation. With the values of resistance and inductance given in Section 2 (200V maximum across coil) the final temperature is almost 1100° K. The assumption of no heat transfer out of the coil is unrealistic, as gas can flow readily through the coil. The final temperature is practically independent of the length of the hot spot, provided this length is much less than the total coil.

If the whole coil goes normal at once, the final temperature is approximately 70 K if it retains all the resistive heat (no cooling). This situation is represented by Fig. 4 which shows the results of a detailed calculation of the temperature and current histories. A computer program solves the differential equations for the currents in the two coils and the temperature of the normal region, assumed to be in one coil (coil #2, the larger one in this case). In order to simulate both coils becoming normal, the value given for the dump resistor R_1 is increased by the resistance of that coil at some average temperature. The value 0.93 ohms is obtained in this case at 54K, the temperature at which one half of the stored energy has been dissipated. Similar results are obtained if the roles of the two coils are reversed. The decay of the current is very rapid (1/λ=19.3 sec) because of the large internal resistance of the coils in the normal state.

The conductor is designed to be thermally stable. The average power density through surfaces exposed to liquid helium is 0.28 w/cm^2 at maximum current in a section of normal conductor. A normal region induced, for example, by frictional heating of a slipping conductor will become superconducting again as soon as the conductor stops moving, if it is under liquid. If a section of conductor becomes normal and stays that way it will rapidly boil helium, blowing it out of the cryostat. The entire coil will then go normal and reach a moderate temperature because of its great heat capacity. If the helium filling system stops working during operation of the magnet, the eventual result would be similar, namely all (or most) of the coil would suddenly go normal after the helium level has dropped far from the top of the coil.

The condition of thermal isolation needed to sustain the hot spot as discussed above is probably not realistic. A similar catastrophe will result if one or several turns became shorted into a closed loop and then the magnet is turned off quickly (e.g. using the dump circuit). A current that can be much larger than the operating value will be induced in the shorted turns and will burn them out. The best protection against this seems to be a conservative design with respect to electrical insulation in the cryostat and avoiding large voltages in the design of the dump circuit. It also suggests that an automatic trigger for the dump circuit may be undesireable. If a short between turns were to occur, the current must be reduced to zero very gradually to prevent damage.

Gas pressure within the coil and cryostat will reach several atmospheres if sufficient heat is produced to boil all the helium in a short time. The excess mechanical strength of the bobbin beyond that needed to support the wire tension is equivalent to a large internal pressure, which seems adequate to insure its safety. The magnetic force on the current in the conductor relieves some of the pressure from the wire on the bobbin, giving an additional increment to the maximum safe pressure while current is flowing.

Reference

1. G. Bronca, J. Krikorian, and J. Neel, Nucl. Inst. & Meth. 79(1970)309.

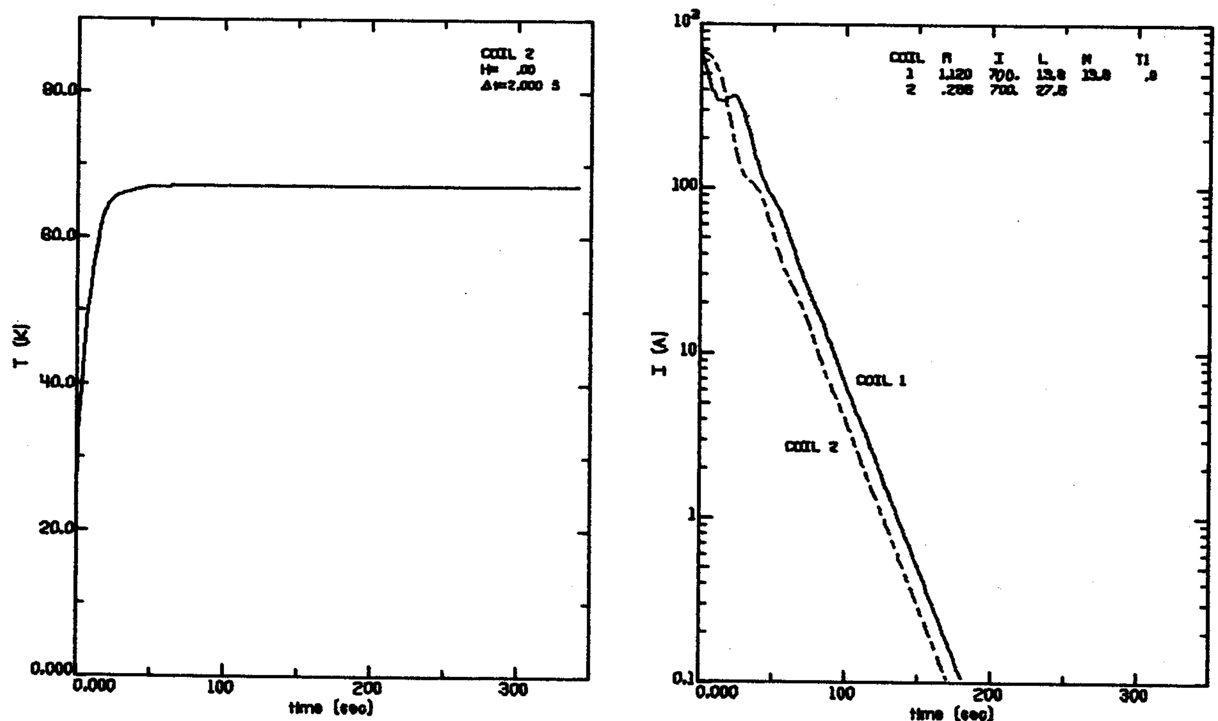

FIG. 4.--Time dependence of the temperature of the normal region (left graph) and currents in the magnet coils (right graph) for conditions representing a sudden transition of the entire magnet coil to the normal state at t=0, accompanied by activation of the dump circuit.

Ion Source

M.L. Mallory, H.G. Blosser, and G. Stork

A program of development and testing of high charge state heavy ion sources is planned for the coming year. The proposed research will be designed to explore ion source behavior in a novel new region of basic parameters, namely, high magnetic field and high vacuum--a region expected to lead to greatly enhanced yields of high charge state ions. High magnetic fields and high vacuum are also characteristics that are of special practical importance in the development of a superconducting cyclotron. The intensity as a function of charge state from the ion source is one of the major uncertainties in evaluating the performance of heavy ion cyclotron systems and Fig. 1 illustrates the importance of the charge parameter from the ion source for a superconducting cyclotron with an energy constant "K" of 500 MeV where the energy per nucleon for different charge number versus mass has been plotted.

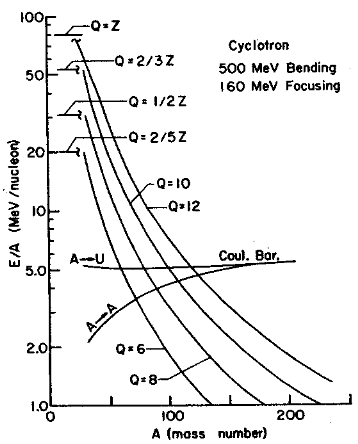

Fig. 1.--Beam energy versus ion mass number for a cyclotron with K=500 MeV. (The cyclotron energy is given by $E=K(Q^2/A)$, where K is the cyclotron energy constant and Q and A are the charge number and mass number of the ion). Curves are given for charge states of 6^+, 8^+, 10^+, and 12^+.

The source testing facility is planned to utilize three major magnets, 1) an existing 46" diameter conventional magnet, 2) the K=55 MeV magnet of the present MSU cyclotron and 3) the K=500 MeV superconducting magnet now being constructed as a part of an MSU cyclotron development program.[1] Ion sources will be designed so that they can be tested or used in any one of these three magnets. The 46" diameter magnet will be equipped as the basic source test-stand with DC voltage for ion extraction. Initial design and debugging of new source features will take place in this test-stand.

When a source is in good DC working order it can be moved to either the 55 MeV magnet or the 500 MeV magnet for further study. In the 55 MeV magnet, rf extraction is available and rf ion source process[2] can be studied. In the 500 MeV magnet, the source would initially be studied using the same DC extraction power supply as the 46" diameter magnet and the main initial goal would be to confirm high magnetic field behavior of the source and develop new source features enhancing their behavior.

One of the promising source features which we plan to study is indirect cathode heating; from the literature indirectly heated cold cathode ion sources appear to give higher yields of high charge states.[3] We therefore plan to build an indirectly heated cold cathode ion source. For axial ion sources it seems advantageous to supply the supplementary cathode heating by rf induction heating. The actual heater will be a small one-turn water cooled coil surrounding the cathode and driven through a coaxial rf feed line by a commercial induction heater.

We also plan to investigate the effects of very strong magnetic fields on the Penning source. In the superconducting magnet, the magnetic pressure will increase enormously (like B^2) leading to longer confinement times and higher electron temperature and density. The production of high charge state ions is thought to be a multiple collision process.[4] Presumably the multiple collision probability should increase like the square of the electron density while loss mechanisms presumably rise only linearly. A strong gain in high charge states therefore seems likely as the field is increased.

The loss of high charge state ions via charge pick-up process has recently been recognized as a serious problem in existing cyclotrons. We plan to investigate the effect of high vacuum on ion output by building a cryopumping system near the ion source so as to investigate ion intensity versus pressure.

Another important line of effort in our study program is to aim at substantially extending the cathode lifetime of the Penning source. As now used Penning sources have a relatively short cathode lifetime and this results in a substantial operating overhead. The axial Penning source geometry offers the opportunity of increasing source lifetimes by making the position of the cathodes remotely movable. (See Fig. 2). A factor of two in lifetimes seems likely and would reduce the source maintenance time accordingly.

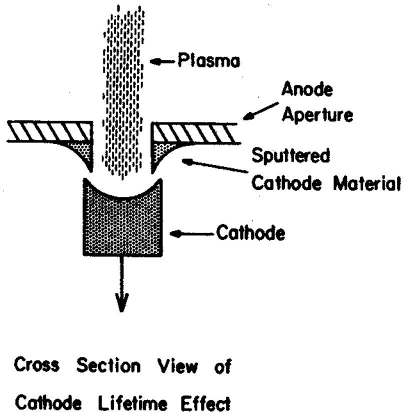

Fig. 2.--Schematic drawing of eroded cathode and sputtered cathode material. The sputtered cathode material builds up in a volcanic cone and eventually shorts to the cathode, causing the arc to "drop out". In the axial Penning ion source, movable cathodes are relatively easy to design. When the arc shorts such a cathode would be backed out of contact with the sputtered material, and the arc could then restrike and continue to operate, thereby increasing the interval between maintenance periods.

An immediate goal of our ion source program is to develop a lithium beam for the MSU cyclotron, using existing source hardware. A drawing of the cold cathode ion source for the MSU cyclotron is shown in Fig. 3. The cathodes are electrically connected and the source body water cooled. A pocket for LiF is located directly behind the ion source extraction slit. The energy of a $^{6}Li^{3+}$ beam from the cyclotron can be as high as 75 MeV and would be of interest to the Nuclear Physics program. In addition the 3^{+} charge state would be less sensitive to the acceleration chamber vacuum than other lithium charge states and one could expect interesting beam intensities.

References

1. H.G. Blosser, D.A. Johnson, R.J. Bürleigh, R.C. Niemann and J.R. Purcell, Seventh International Conference on Cyclotron and Their Applications, Berkhauser (1975) 584.

2, E.D. Hudson, M.L. Mallory, R.S. Lord, IEEE Trans. Nucl. Sci., NS-23 No. 2, (1976) 1065.

3. B.N. Makov, IEEE Trans. Nucl. Sci., NS-23, No. 2 (1976) 1035.

4. G. Fuchs, IEEE Trans. Nucl. Sci., NS-19, No. 2 (1972) 160.

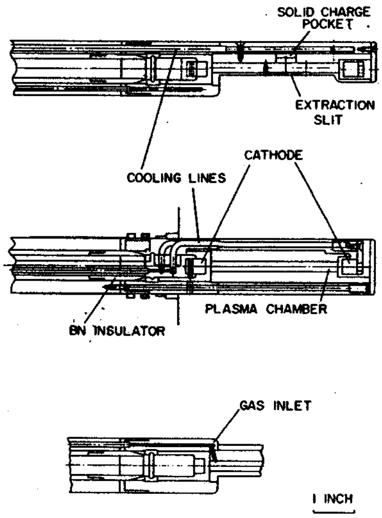

Fig. 3.--A modification of the existing MSU cold cathode ion source is shown. The two cathodes are electrical connected by water cool tubes. The ion source can be completely disassembled for maintenance without breaking any water and vacuum seals. A pocket for solid charge materials is provided directly behind the ion source extraction slit.

ADDENDUM:

On September 16, 1976, a 70 MeV beam of $^{12}C^{4+}$ at an intensity of 3.5 eμA was extracted from the cyclotron using the heavy ion source described above. Shortly thereafter, beams of 98 MeV $^{14}N^{5+}$ at an intensity of 1 eμA, 35 MeV $^{6}Li^{2+}$ at an intensity of 3 eμA, and 72 MeV $^{6}Li^{3+}$ at an intensity of 15 enA were also extracted. An experimental program using these beams started on September 20, 1976. With further experience, ion source change times (i.e. the time to change the cathodes and restrike the arc) of less than 15 minutes appear feasible.

Injection Orbits from a Tandem into a Superconducting Heavy-Ion Cyclotron

J.N. Bishop

We have studied orbits for injection of ions from 13 MeV and 25 MeV tandems into the prototype superconducting cyclotron magnet. A useful parameter for characterizing the orbits is:

$$R = \frac{E_2/E_1}{\left(\frac{2Q_2}{Q_1} - 1\right)^2}$$

where E_1 is the energy of the charge Q_1 ion from the tandem which is stripped to charge Q_2 in the cyclotron and accelerated to energy E_2. For a uniform magnetic field with a hard circular edge $R \leq 1$. We have found that for our magnet there are no injection orbits with $R > 0.9$.

Orbits were calculated starting from the stripper foil at the hill center and for a ±20° range about the hill center and integrated backwards to the radius 36". Fig. 1 shows the azimuth at 36" as a function of R for a wide variety of ions from a 13 MeV tandem. Two injection ports at $\theta_{r=36"} = 279°$ and 302° can cover well the range in R from 0.30 to 0.79. Fig. 2 shows that the injection orbits through these two ports have the desirable property of not running along the edge of a hill where the magnetic field gradient is large and where the RF field is present.

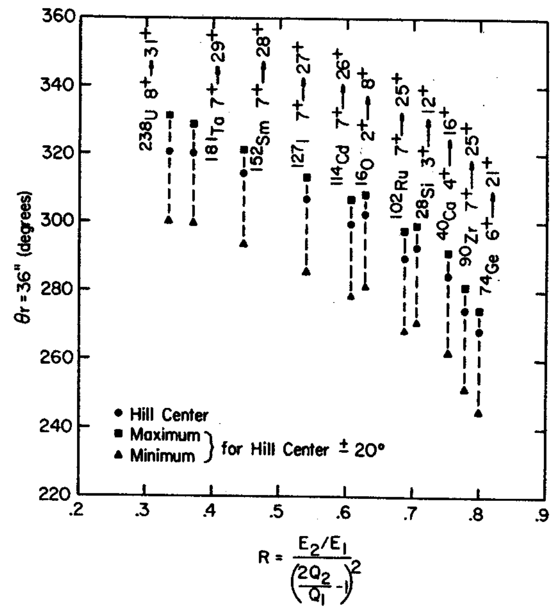

Fig. 1.--Azimuth at the magnet exterior (r=36") necessary for injection with the stripper located along a hill center (±20°) for a variety of ions from a 13 MeV tandem.

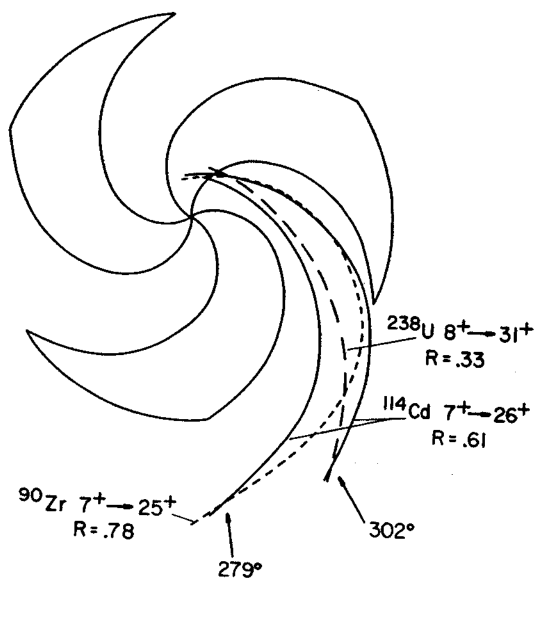

Fig. 2.--Injection orbits passing through the points r=36", θ=279° and r=36", θ=302°.

Beam Extraction Studies for a $E=500(q^2/A)$ MeV Superconducting Cyclotron

M. Gordon, H. Blosser, D. Johnson, and F. Marti

Beam extraction from a superconducting cyclotron poses difficult problems because of the very high magnetic fields. Significant progress toward solving these problems has been made in the year since the last report on this work.[1] Results obtained from our most recent extraction design studies are shown in Fig. 1.

These designs make use of "focusing bars" which produce a quadrupole focusing effect through a special configuration of iron bars, suggested to us by C. Hoffman at Chalk River. This novel design element, which is shown in Fig. 2, provides much needed radial focusing during extraction. Calculations indicate that the focusing bars will produce a 5 kG/in gradient in our magnet situation.

At present, our preferred extraction design consists of three electrostatic deflectors together with three sets of focusing bars, as shown in the top part of Fig. 1. This arrangement avoids the difficulties in placing high voltage electrodes inside the dees. Moreover, the use of three deflectors provides the system with added flexibility.

Results from orbit computations displayed in the top part of Fig. 1 indicate that a beam which enters the system with a 2 mm x 3 mrad emittance will emerge with a final radial width of 12 mm. This is rather good considering the 4.3 meter flight path of the beam through what would otherwise be a highly defocusing magnetic field.

For comparison, the lower part of Fig. 1 shows results for an alternate design with the third electrostatic deflector replaced by a "supertube". This device is a superconducting Nb_3Sn tube designed at Stanford,[2] which provides an almost perfect magnetic shield with $B\approx0$ inside. The supertube with its cryostat requires about 2 inches for comfortable beam clearance, so that this design would utilize the first two electrostatic deflectors to generate this clearance. As indicated in Fig. 1, the beam for this case, would have a shorter path within the field and would then emerge with a radial width of only 6 mm.

The calculations used to construct Fig. 1 have ignored the effects of the field penetration near the ends of the supertube. Since the 0.64 inch aperture is small compared to the 15 inch length of the tube, these end effects are probably small. To investigate this question more fully, we are carrying out a series of calculations based on a surface current distribution along the tube given by:

$$dI_x = (2aB/\mu_o)(\cos\phi + g\cos2\phi)d\phi,$$

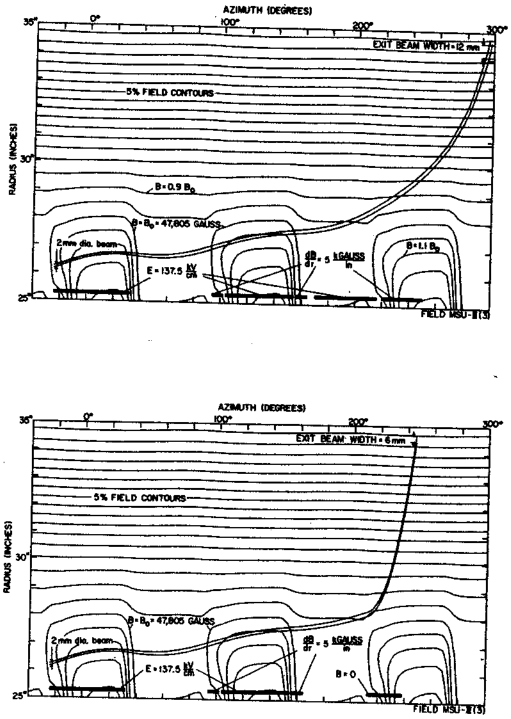

Fig. 1.--Plots of r(inches) versus θ(deg) for orbits of ions having E/A=49.4 MeV and q/A=0.31 tracked through two possible extraction systems (top and bottom). In both cases, the two curves give the envelope of a set of orbits which start out at θ=-24° on an emittance rectangle of dimensions 2 mm x 3 mrad. Shown in the background are the isogauss contour lines which range from $B=0\,1.2B_o$ on the three hills near r=25" down to $B=0.15B_o$ near r=35", where B_o=47.8 kG here. The top and bottom drawings are identical in the region between θ=-24° and θ=170° where the orbits pass through two electrostatic deflectors (θ=-24° to +32° and θ=104°-154°) having 137.5 kV/cm field strength, and through two sets of "focusing bars" (θ=94°-102° and θ=156°-164°) having 5 kG/in transverse gradient. In the preferred system shown at top, the ions then pass through a third electrostatic deflector (θ=170°-216°) and then a third set of focusing bars (θ=220°-250°), and finally reach r=34.4" at θ=300" with a radial beam width of 12 mm. For the alternative scheme shown at bottom, in place of the third deflector and focusing bars, the ions pass through a "supertube" (θ=212°-238°) where B=0, and finally emerge at r=34.4" (θ=246°) with a radial width of only 6 mm. Note that the orbits pass through one dee in the first magnet valley (θ=33°-93°) and then run outside the dee in the next valley.

where $\underline{a}$ is the supertube radius and ϕ is measured from the midplane ($z=\underline{a}\sin\phi$). Here, B is the external field and $g=aB'/B$, where B' is the field gradient across the tube. We estimate that $g\approx0.1$ in our case.

The above current is valid for an infinite tube, and to close the circuit for a finite tube, we assume the integrated current flows across the tube end. This end-current is then given by:

$$I_\phi = (2aB/\mu_0)(\sin\phi + 1/2g\ \sin 2\phi),$$

and is depicted in Fig. 3 for the case where g=0. Although this type of current distribution is only approximately correct, it is sufficiently simple to make the resultant field calculations fairly reasonable. Fig. 4 shows, for example, the field along the supertube axis produced by the current shown in Fig. 3. We plan to use such field calculations to evaluate the resultant beam focusing and aberration effects.

The Stanford group has kindly supplied us with a sample supertube, and we have successfully operated this device in the edge region of a large spectrograph magnet and have verified that B is very small inside the tube. Although these results are encouraging, the operation of supertubes is not sufficiently reliable as yet to warrant its use in our present design. Consequently, the cryostat for the superconducting magnet now under construction has been designed to accommodate the more conventional extraction system described above. Nevertheless, experimental and theoretical work on the supertube will be continued in the hope that this device can be perfected for use in a future superconducting cyclotron.

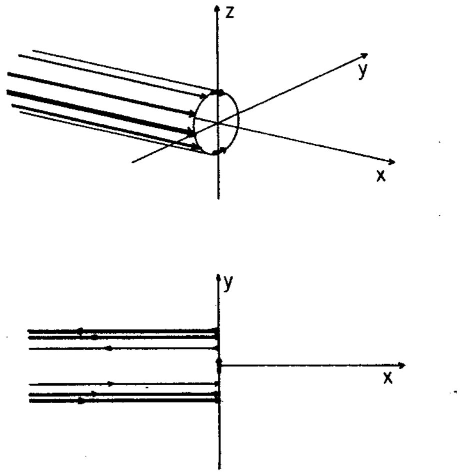

Fig. 3.--Surface current distribution near the end of a supertube. Upper drawing shown side view in perspective, while lower drawing shows top view of the current.

References

1. H. Blosser, "Superconducting Cyclotrons", Proc. Seventh International Cyclotron Conf., 1975.

2. F. Martin, S. St. Lorant, and W. Toner, Nucl. Instr. and Meth. 103,503(1972).

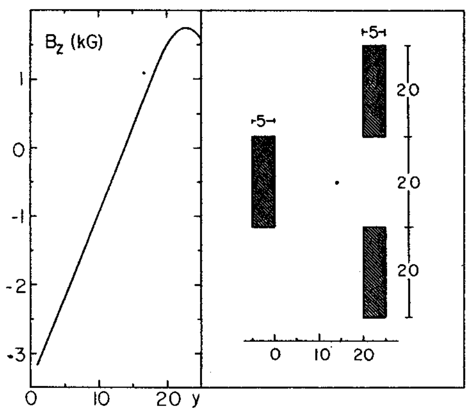

Fig. 2.--Median plane magnetic field B_z produced by three magnetized iron bars shown in cross-section at right. The black dot at y=14 indicates the beam center (B_z=0). The plot at left gives B_z in kG versus y in an arbitrary length unit which determines the focusing gradient at the beam center. If, for example, y=20=20 mm, then this gradient is 6.3 kG/inch. The calculations assumed a uniform vertical magnetization of the bars corresponding to an internal field of 21.4 kG.

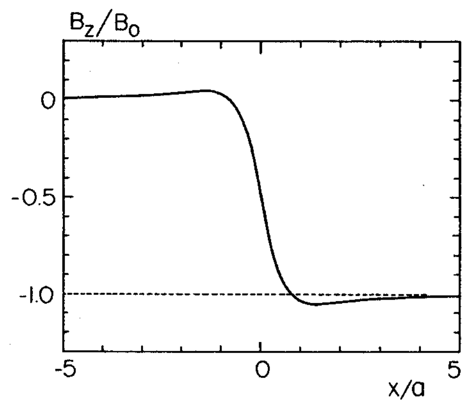

Fig. 4.--Magnetic field B_z along supertube axis (x-axis) produced by the surface current shown in Fig. 3 plus the external Field B_0. The tube radius is a.

Cyclotron Instrumentation

P. Miller, H. Blosser, W.S. Chien, J.F.P. Marchand, and G. Stork

1. Internal Beam Phase Probe

A probe for measuring the phase of the cyclotron beam anywhere on the radius interval between 3" and the full energy radius, 29.5", has recently become operational. A thin coating of MgO (scintillator) deposited on a water cooled copper target intercepts the cyclotron beam at the probe tip. The resulting light pulse is directed by a pair of mirrors along the axis of the probe to a photomultiplier outside the cyclotron. The photomultiplier anode pulse and a reference marker derived from the dee voltage zero crossing are displayed on a 2-channel sampling oscilloscope (Tektronix 3576/RM564) which is interfaced to the PDP 11/20 computer used for cyclotron control. The computer averages a number of oscilloscope sweeps and derives the phase shift between the two signals by a fitting procedure. The result of making such a measurement at a number of probe positions is a phase curve (see examples) in Fig. 1.

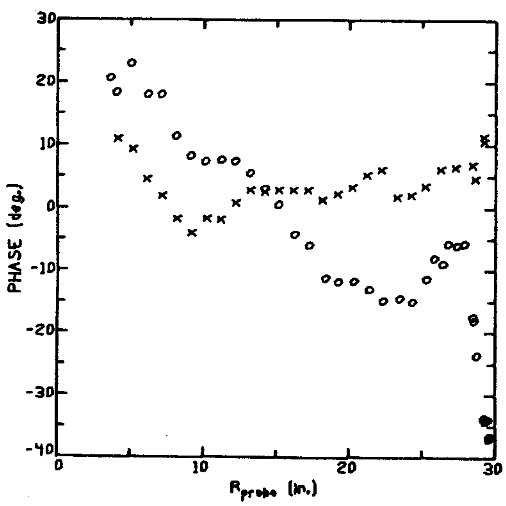

Fig. 1 Beam phase vs. probe radius for 27 MeV $^3He^{++}$ ions before correction (circles) and after one correction pass (crosses).

The instrument has no energy threshold, which is the major deficiency of the standard gamma-ray time of flight methods of phase measurement. In fact, the signals are largest at low beam energy.

Since it intercepts the beam, the probe can measure one turn at a time. By contrast, phase measuring methods that use direct capacitive or inductive pickup give an everage over several turns. Also, such devices would be more susceptible to pickup of the rf signal.

2. Phase Width Monitor

A gamma-ray detector with good timing characteristics has been assembled to measure the phase width of the cyclotron beam. It has been used to check the proton beams used for neutron time of flight experiments. A typical width measured on the beam stop at the cyclotron exit is .37 nsec. FWHM (2.3 rf degrees) for 35 MeV protons, shown in Fig. 2. The two peaks represent a 4 nsec. change in the time delay of the reference (stop) signal (for calibration). The apparatus is diagrammed in Fig. 3.

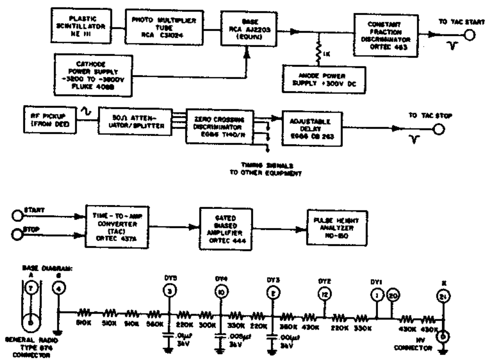

Fig. 3 Block diagram of the phase width measuring apparatus.

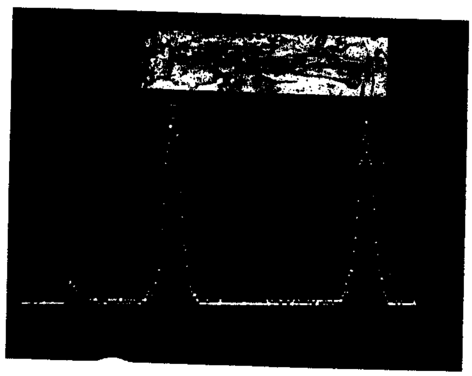

Fig. 2 Two superimposed gamma-ray time spectra with 4 nsec. change of delay for calibration. Peak width is 0.37 nsec. FWHM.

Time spectra under conditions similar to those for Fig. 2 have shown a peak width as small as .34 nsec. In tests using a ^{60}Co γ-ray source and a similar detector in coincidence as a timing reference, the time resolution was .25 nsec FWHM. The energy threshold was lowered for this test. Assuming that the two detectors dontribute equally and in quadrature to this width, the single detector electronic resolution limit is .18 nsec FWHM. Subtracting this in quadrature from the .37 nsec shown above gives .33 nsec (2.1 degrees) as the cyclotron beam phase width.

3. Tests of Devices for Superconducting Cyclotron

The transfer of proven designs for cyclotron parts, for example the electrostatic deflector and beam probe, to the superconducting cyclotron will require some miniaturization and other changes of the devices. The present cyclotron is being used to test these modifications.

3.1. Electrostatic Deflector

The electrostatic deflector high voltage electrode was replaced with one designed to fit in the reduced magnet gap. It differs by the absence of water cooling and a smaller cross section area (see Fig. 4). After testing small model sections made of carefully polished hard chrome plated copper, inconel, and 304 stainless steel and obtaining equally satisfactory sparking performance from all samples, we chose stainless steel as the material for building the prototype, based on cost of material, machining ease and amount of radiation exposure to maintenance personnel from induced radioactivity. A final sample was commercially polished using standard buffing techniques and also held voltage well, so the prototype was made in this way. The electrode has been used in the cyclotron continuously for 4 months. It has been found to hold 95 kV in conditioning tests. The highest voltage used so far in actual cyclotron operation is 89 kV.

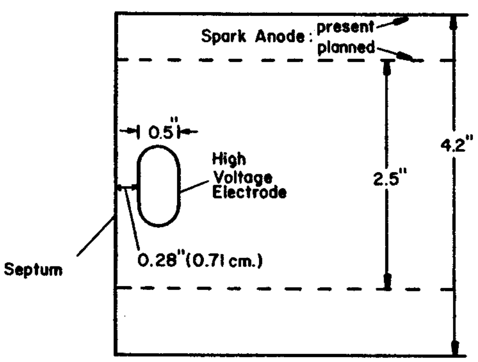

Fig. 4 Cross section of deflector assembly. The septum and the spark anode plates are 0.020" (0.5 mm) thick tungsten.

The 3 alumina supporting insulators in the old design have been replaced by 2 smaller boron nitride insulators and a metal tension rod which also serves as the connection to the power supply. After three months one insulator broke down at high voltage and required replacement. The apparent cause was surface contamination from the vacuum system.

Tests of this deflector with the tungsten spark anodes moved closer to the median plane are planned (see Fig. 4). (Note: In the first conditioning test a potential of 93 kV was reached.)

3.2. Beam Sensing With Secondary Electrons

A differential beam probe consisting of two overlapping water-cooled targets which can stop the beam is the normal diagnostic probe used for tuning the MSU cyclotron. Such a device would be desirable in the superconducting cyclotron, but its sensitivity to the beam direction dictates that it move along a magnetic symmetry line, such as the center of a hill. The large spiral in the new magnet would imply that the probe would be mechanically complicated.

In order to get the same information from a radially-moving probe, we have built and tested successfully a probe with a 0.5 mil (.013 mm) dia. tungsten wire as the differential electrode. The current signal comes from secondary electrons leaving the wire, which was inclined slightly with respect to the magnetic field to avoid recapture of the electrons on the wire support posts. The yield of secondary electrons is seen to increase with energy (see Fig. 5). A thin wire is necessary to prevent overheating, since the wire is cooled only by radiation.

A non-intercepting secondary electron monitor for position sensing which uses the residual gas as the target has been installed in the cyclotron at the exit port of the magnetic channel to measure the sensitivity and check the feasibility of such a system for sensing the position of the beam in the extraction channel. A clearing field of about 2 v/cm produces saturation of the signal. Using plates that are 5.08 cm along the beam direction and wide enough to cover the orbit, we obtained the data shown below. The pressure was estimated from the gas flow rate to the ion source and the estimated conductance of the structures in the magnet gap.

ion	Beam energy [MeV]	Beam current [eμA]	Electron current [pA]	Pressure [μTorr]	Sensitivity [pA/μTorr-eμA-cm]
$^{12}C^{+3}$	30	.24	120	14	7
$^{1}H^{+}$	12	5	280	30	.4
*	35	.48	800	250	1.3

*** Measured in a magnet separate from the cyclotron.**

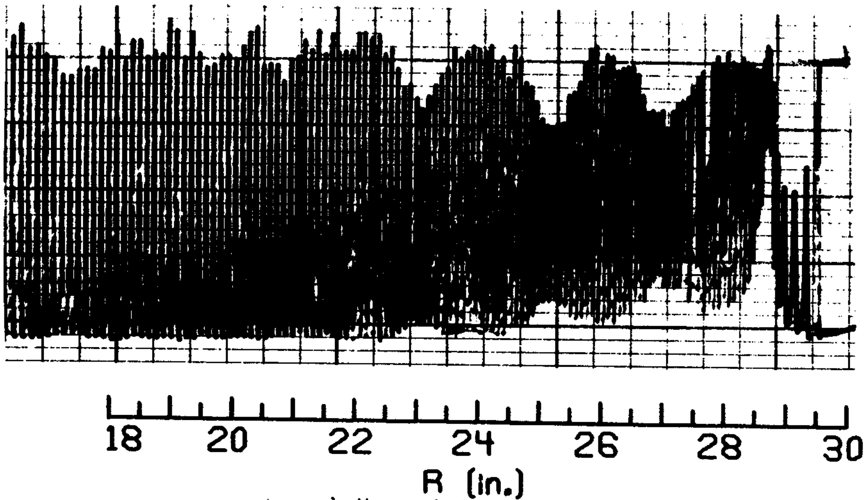

a) Normal beam probe

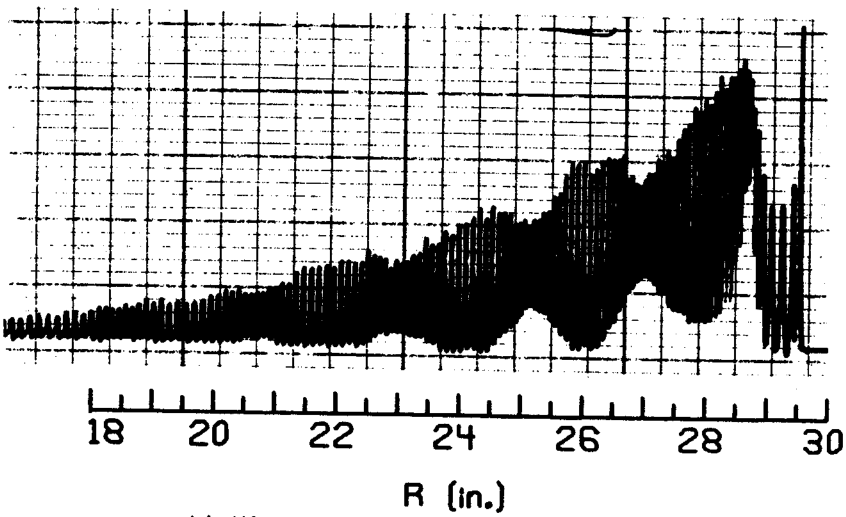

b) Wire probe (0.5 mil dia. tungsten)

Fig. 5.--Differential probe traces showing the turn structure in the MSU Cyclotron running protons to 35 MeV.